




Article

# Porous Carbon Spheres Derived from Hemicelluloses for Supercapacitor Application

Yuanyuan Wang <sup>1</sup>, Chengshuai Lu <sup>1</sup>, Xuefei Cao <sup>1,2,\*</sup>, Qiang Wang <sup>1</sup>, Guihua Yang <sup>1</sup>  and Jiachuan Chen <sup>1,\*</sup>

<sup>1</sup> State Key Laboratory of Biobased Material and Green Papermaking, Qilu University of Technology, Shandong Academy of Sciences, Jinan 250353, China; wyy1989zyc@163.com (Y.W.); lcs011129@163.com (C.L.); wangqiang8303@163.com (Q.W.); ygh2626@126.com (G.Y.)

<sup>2</sup> Beijing Key Laboratory of Lignocellulosic Chemistry, Beijing Forestry University, Beijing 100083, China

\* Correspondence: caoxuefei@bjfu.edu.cn (X.C.); chenjc@qlu.edu.cn (J.C.); Tel.: +86-010-62336903 (X.C.)

**Abstract:** With the increasing demand for dissolving pulp, large quantities of hemicelluloses were generated and abandoned. These hemicelluloses are very promising biomass resources for preparing carbon spheres. However, the pore structures of the carbon spheres obtained from biomass are usually poor, which extensively limits their utilization. Herein, the carbon microspheres derived from hemicelluloses were prepared using hydrothermal carbonization and further activated with different activators (KOH, K<sub>2</sub>CO<sub>3</sub>, Na<sub>2</sub>CO<sub>3</sub>, and ZnCl<sub>2</sub>) to improve their electrochemical performance as supercapacitors. After activation, the specific surface areas of these carbon spheres were improved significantly, which were in the order of ZnCl<sub>2</sub> > K<sub>2</sub>CO<sub>3</sub> > KOH > Na<sub>2</sub>CO<sub>3</sub>. The carbon spheres with high surface area of 2025 m<sup>2</sup>/g and remarkable pore volume of 1.07 cm<sup>3</sup>/g were achieved, as the carbon spheres were activated by ZnCl<sub>2</sub>. The supercapacitor electrode fabricated from the ZnCl<sub>2</sub>-activated carbon spheres demonstrated high specific capacitance of 218 F/g at 0.2 A/g in 6 M KOH in a three-electrode system. A symmetric supercapacitor was assembled in 2 M Li<sub>2</sub>SO<sub>4</sub> electrolyte, and the carbon spheres activated by ZnCl<sub>2</sub> showed excellent electrochemical performance with high specific capacitance (137 F/g at 0.5 A/g), energy densities (15.4 Wh/kg), and good cyclic stability (95% capacitance retention over 2000 cycles).

**Keywords:** hemicelluloses; carbon microspheres; hydrothermal carbonization; supercapacitor



**Citation:** Wang, Y.; Lu, C.; Cao, X.; Wang, Q.; Yang, G.; Chen, J. Porous Carbon Spheres Derived from Hemicelluloses for Supercapacitor Application. *Int. J. Mol. Sci.* **2022**, *23*, 7101. <https://doi.org/10.3390/ijms23137101>

Academic Editor: Suresh Valiyaveetil

Received: 2 June 2022

Accepted: 23 June 2022

Published: 26 June 2022

**Publisher's Note:** MDPI stays neutral with regard to jurisdictional claims in published maps and institutional affiliations.



**Copyright:** © 2022 by the authors. Licensee MDPI, Basel, Switzerland. This article is an open access article distributed under the terms and conditions of the Creative Commons Attribution (CC BY) license (<https://creativecommons.org/licenses/by/4.0/>).

## 1. Introduction

In recent years, with the increasing consumption of petrochemical resources and the deterioration in environmental pollution, more and more attention has been paid to the development of renewable and sustainable energy storage devices. The main application power sources include supercapacitors, fuel cells, lithium-ion batteries, etc., among which, supercapacitors are one of the most promising electrochemical energy storage devices due to their high power density and short charging and discharging time [1,2]. Supercapacitors can be divided into pseudocapacitors and electric double-layer capacitors (EDLC) according to the charge storage mechanisms. EDLC have many advantages, such as superior stability and long cycle life, which make them attractive power sources for emergency power supply systems, hybrid cars, portable electronic devices, etc. [3,4]. However, the low energy density of supercapacitors (<10 Wh/kg) limits their practical application [5]. In addition, the application scope and electrochemical performance of the supercapacitors are influenced by the price and properties of the electrode materials to a certain extent. Therefore, more and more researchers have concentrated on improving the properties of electrode materials to enhance the electrochemical performance of supercapacitors [6–8].

Carbon materials, such as carbon fiber, graphene, and carbon microspheres, have the advantages of strong chemical stability and good electrical conductivity, making them a good choice for electrode materials in supercapacitors [9–12]. Numerous works

found that electrode materials with large specific surface area and abundant pore structure can increase the storage of the electrolyte and reduce the transmission resistance of electrolyte ions, which is beneficial for improving the electrochemical performance of supercapacitors [13–16]. Porous carbon spheres are usually considered as preferable electrode materials due to their regular shape, large specific surface area, low surface free energy, and high packing density [17,18]. The porous carbon spheres are mainly prepared from nonrenewable and expensive petroleum-based resources, such as styrene, toluene, benzene, pitch, etc. [19]. Recently, hydrothermal carbonization of biomass has been one of the most attractive routes for the preparation of carbon, since this method is green, simple, and eco-friendly [18,20]. Among various biomass resources for preparing carbon spheres, hemicelluloses are very promising because they are considered as the second most abundant renewable resource only after cellulose. Furthermore, they are cheap, easy to extract, and usually treated as by-products of pulp and paper industry. However, the pore structures of the carbon spheres obtained by hydrothermal carbonization of biomass are usually poor, which extensively limits the utilization of these carbon spheres as electrode materials [21,22]. Therefore, it is necessary to improve the surface properties and pore structures of these carbon spheres to obtain good electrode materials with excellent electrochemical performance [23,24]. It is well known that physical activation and chemical activation are the main activation methods for carbon materials. Among them, chemical activation is a very effective method due to its low activation temperature, short activation time, and high yield of carbon materials. Many reagents, such as KOH, ZnCl<sub>2</sub>, H<sub>3</sub>PO<sub>4</sub>, K<sub>2</sub>CO<sub>3</sub>, NaOH, etc., can be used as activators for chemical activation. Among these activators, KOH, ZnCl<sub>2</sub>, and H<sub>3</sub>PO<sub>4</sub> are the most commonly used [25]. The carbon materials obtained from chemical activation contain a large number of micropores and mesopores, which is beneficial for improving the electrochemical performance [26,27]. Rey-Raap et al. explored the influence of carbon nanotubes addition in biomass-derived carbon materials, and a KOH-activated glucose-derived carbon material was prepared by hydrothermal carbonization of glucose in the presence of carbon nanotubes [28]. Results showed that the assembled supercapacitor had a high specific capacitance of 206 F/g at a current density of 0.2 A/g when only 2 wt% of carbon nanotubes was added. Fan et al. prepared a series of micro-mesoporous carbon spheres by hydrothermal carbonization of carrageenan and further activated by KOH at different temperatures, and a high specific capacitance of 230 F/g (current density 1 A/g) was achieved from the carbon spheres activated at 900 °C [29].

In this work, carbon spheres were prepared from the industrial hemicelluloses with high purity and uniform structures extracted from the dissolving pulp by hydrothermal carbonization [30]. Then, various activating reagents, such as KOH, K<sub>2</sub>CO<sub>3</sub>, Na<sub>2</sub>CO<sub>3</sub>, and ZnCl<sub>2</sub>, were used to activate the carbon spheres to improve the electrochemical performance of these hydrothermal carbon spheres as electrode materials. The structure and properties of these carbon spheres were investigated with scanning electron microscopy (SEM), X-ray photoelectron spectroscopy (XPS), N<sub>2</sub> adsorption/desorption, and Raman spectroscopy. Furthermore, the activated carbon spheres were used as electrode materials in supercapacitors to evaluate their electrochemical performances.

## 2. Results and Discussion

### 2.1. Preparation of the Hydrothermal Carbon Spheres

Previous work showed that the hemicelluloses extracted from the dissolving pulp mainly comprised (1→4)-linked β-D-xylans, which is a good raw material for producing carbon spheres by hydrothermal carbonization [30]. In this work, the hydrothermal carbonization of the hemicelluloses was performed in 2% H<sub>2</sub>SO<sub>4</sub> solution because the addition of acid could promote the degradation of hemicelluloses into furan compounds and significantly improve the yield of carbon spheres [15,31]. As compared with the carbon sphere yield of 33.9% obtained from water, a much higher carbon spheres yield of 44.6% was achieved when the hydrothermal carbonization was carried out in 2% H<sub>2</sub>SO<sub>4</sub> solution. The morphology of the hydrothermal carbon spheres was detected with SEM and shown

in Figure 1. The hydrothermal carbon spheres prepared in 2%  $\text{H}_2\text{SO}_4$  solution were more regular and smooth.

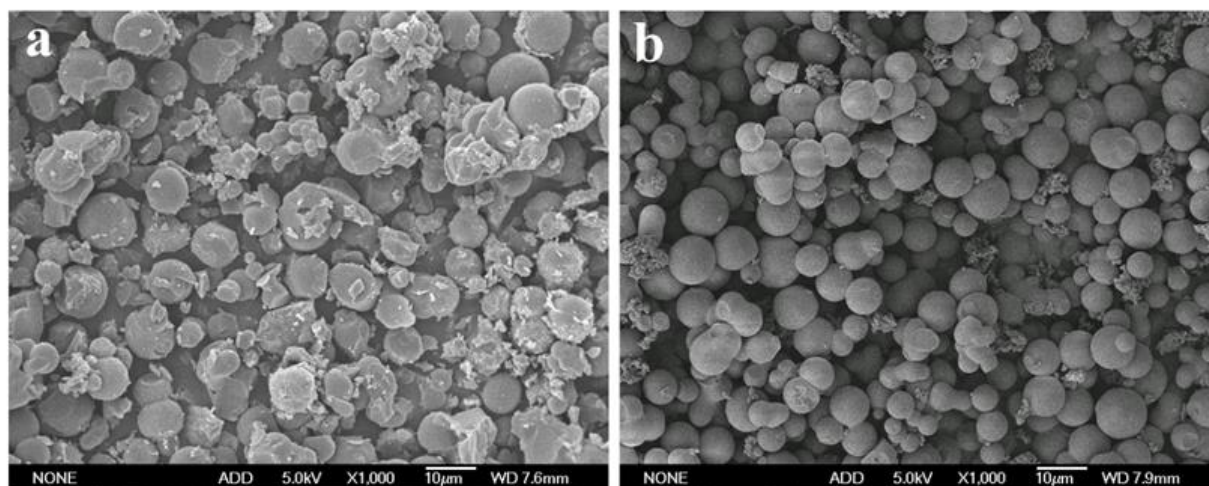


**Figure 1.** SEM images of the hydrothermal carbon spheres derived from hemicelluloses in (a) water and (b) 2%  $\text{H}_2\text{SO}_4$  at 180 °C for 12 h at a magnification of 1000 $\times$ .

## 2.2. Preparation and Characterization of the Activated Carbon Spheres

Generally, the carbon materials obtained from hydrothermal carbonization show poor specific surface area and porosity, which makes it difficult for them to meet the requirements of supercapacitors [15,21]. In this work, four activators, including KOH,  $\text{K}_2\text{CO}_3$ ,  $\text{ZnCl}_2$ , and  $\text{Na}_2\text{CO}_3$ , were used to improve the pore structure and specific surface area of the hydrothermal carbon spheres. The activated carbon spheres without the addition of the activator were recorded as ACS, and the carbon spheres activated with KOH,  $\text{K}_2\text{CO}_3$ ,  $\text{Na}_2\text{CO}_3$ , and  $\text{ZnCl}_2$  were recorded as ACS-KOH, ACS- $\text{K}_2\text{CO}_3$ , ACS- $\text{Na}_2\text{CO}_3$ , and ACS- $\text{ZnCl}_2$ , respectively. Figure 2 shows the SEM images of these activated carbon spheres (ACS, ACS-KOH, ACS- $\text{K}_2\text{CO}_3$ , ACS- $\text{Na}_2\text{CO}_3$ , and ACS- $\text{ZnCl}_2$ ). It can be seen that the surface of ACS was still smooth, and the morphology of ACS hardly changed during the calcination process. However, the surface of ACS-KOH, ACS- $\text{K}_2\text{CO}_3$ , ACS- $\text{Na}_2\text{CO}_3$ , and ACS- $\text{ZnCl}_2$  became rough. Among them, the spherical shape of ACS-KOH was seriously damaged. Similar results were also observed in the KOH-activated carbon materials derived from glucose, and it was stated that the obvious etched morphology was correlated with the fusion of KOH drops on the surface or the formation of a liquid-phase intermediate during activation [28,32]. It is worth noting that although many pores were observed in the SEM images of ACS-KOH, these pores were mainly macropores. Mesopores and micropores can rarely be observed in SEM images because of their small sizes. Therefore, the mesopores and micropores of the samples were further characterized by  $\text{N}_2$  adsorption and desorption measurement.

The electrochemical performances of carbon materials are significantly affected by their porous structures. The specific surface area and pore volume of these carbon spheres are shown in Table 1. As compared with the ACS, the Brunauer-Emmett-Teller (BET)-specific surface area of these activated carbon spheres increased significantly, which was in the order of ACS- $\text{ZnCl}_2$  > ACS- $\text{K}_2\text{CO}_3$  > ACS-KOH > ACS- $\text{Na}_2\text{CO}_3$ . Similar trend was also observed from the pore volume results. Therefore, the porous structure of the carbon materials is closely related to the activators used. Among these activated carbon materials, the specific surface area of ACS- $\text{ZnCl}_2$  (2025  $\text{m}^2/\text{g}$ ) was much higher than others (441–1141  $\text{m}^2/\text{g}$ ). The  $\text{N}_2$  adsorption/desorption isotherms of these carbon spheres are shown in Figure 3a. Typical type I isotherms were observed for all carbon sphere samples, and no obvious hysteresis loops were found. However, for ACS- $\text{K}_2\text{CO}_3$ , ACS-KOH and ACS- $\text{Na}_2\text{CO}_3$  samples, the adsorption amount of  $\text{N}_2$  still gradually increased with the increment of  $P/P_0$  from 0.20 to 0.95, indicating that in addition to micropores, a small



amount of mesopores existed in these activated carbon spheres. From the isotherm of ACS-ZnCl<sub>2</sub>, it was found that the adsorption amount of N<sub>2</sub> significantly increased with the increment of P/P<sub>0</sub> from 0.05 to 0.40 and then tended to be flat. It suggested that a relatively high content of mesopores but in small size was contained in the ACS-ZnCl<sub>2</sub> sample [16,33,34]. Due to the difference of the activation mechanism, the porous structure of the carbon materials activated by different activators may have varied significantly. Heidarinejad et al. stated that potassium metal is thought to be introduced into the internal structure of the carbon matrix during the gasification process, leading to the expansion of existing pores and the creation of new ones [35]. For Zn ions, Rupa et al. reported that evaporation of carbo-thermally reduced Zn was known to be crucial in the zinc activation mechanism, as it caused the interlayer movement of zinc ions inside a carbon scaffold, which could further enhance pore development by internal tunnel formation [36]. Meanwhile, Heidarinejad et al. stated that ZnCl<sub>2</sub> could enhance the condensed aromatic reactions by facilitating molecular hydrogen deformation from the hydro-aromatic structure of the precursors [35]. By increasing the amount of ZnCl<sub>2</sub>, more cracks may occur in the structure of activated carbon and result in the mesoporosity increase in the activated carbon structure, which further breaks down, and the micropores deform to form mesopores [35]. Moreover, the molecular size of the metallic salts intercalated in the carbon layers removed during the washing stage may also be responsible for their porosity and pore sizes [37,38]. Figure 3b shows the pore size distribution diagram of these carbon spheres calculated by the density functional theory (DFT) model. Results suggested that ACS presented a high ratio of micropores, while ACS-KOH, ACS-K<sub>2</sub>CO<sub>3</sub>, ACS-Na<sub>2</sub>CO<sub>3</sub>, and ACS-ZnCl<sub>2</sub> also contained some smaller mesopores in addition to micropores. Notably, the pore sizes of ACS-ZnCl<sub>2</sub> were mainly centered at 1–2 and 2–4 nm, indicating that ZnCl<sub>2</sub> can significantly promote the formation of mesopores. The existences of these mesopores were conducive to the storage of charge and electrolyte, which can significantly accelerate the transport of electrolyte ions [39,40]. Therefore, these activated carbon spheres may have excellent electrochemical performances, especially ACS-ZnCl<sub>2</sub>.

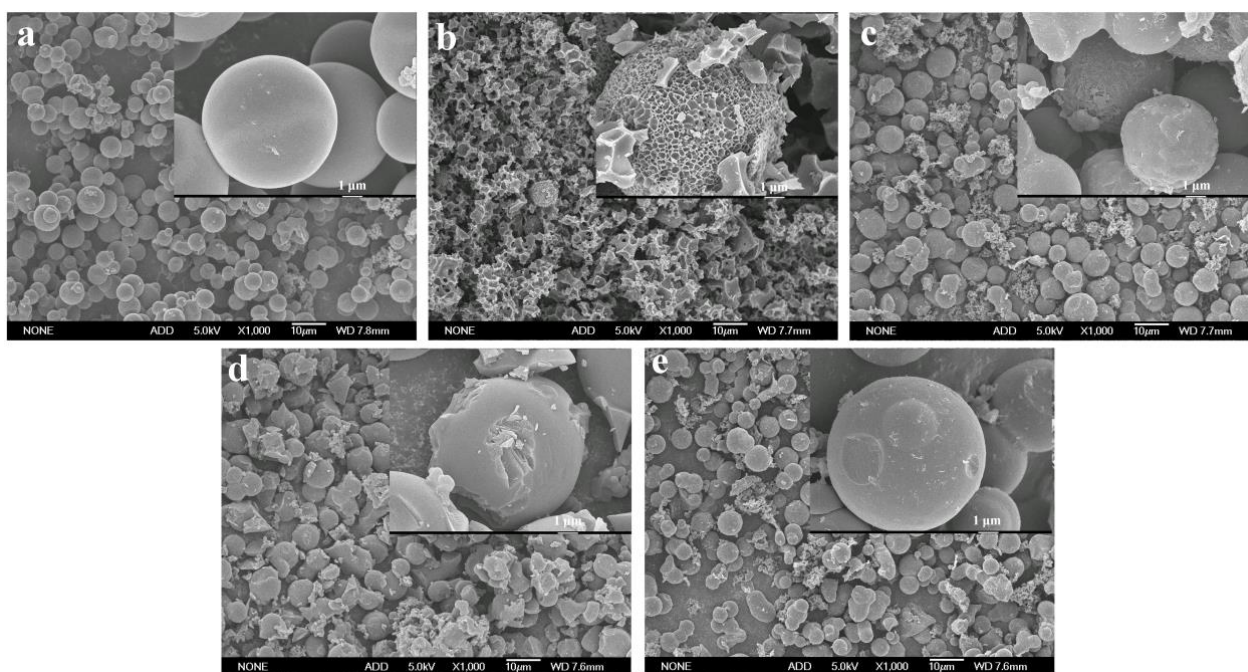


**Figure 2.** SEM images of (a) ACS, (b) ACS-KOH, (c) ACS-K<sub>2</sub>CO<sub>3</sub>, (d) ACS-ZnCl<sub>2</sub>, and (e) ACS-Na<sub>2</sub>CO<sub>3</sub> at a magnification of 1000× and 10,000×, respectively.

**Table 1.** The BET-specific surface areas, pore volume, surface element composition, and specific capacitance in three-electrode system of the carbon spheres activated with different activators.

Sample	ACS	ACS-KOH	ACS-K <sub>2</sub> CO <sub>3</sub>	ACS-Na <sub>2</sub> CO <sub>3</sub>	ACS-ZnCl <sub>2</sub>
BET-specific surface areas (m <sup>2</sup> /g)	441	852	1141	782	2025
Pore volume (cm <sup>3</sup> /g)	0.27	0.50	0.66	0.44	1.07
C (at.%)	96.27	93.44	86.55	93.68	94.11
O (at.%)	3.73	6.56	13.45	6.32	5.89
specific capacitance <sup>1</sup> (F/g)	98	149	172	128	183

<sup>1</sup> The specific capacitance was obtained by galvanostatic charge–discharge (GCD).

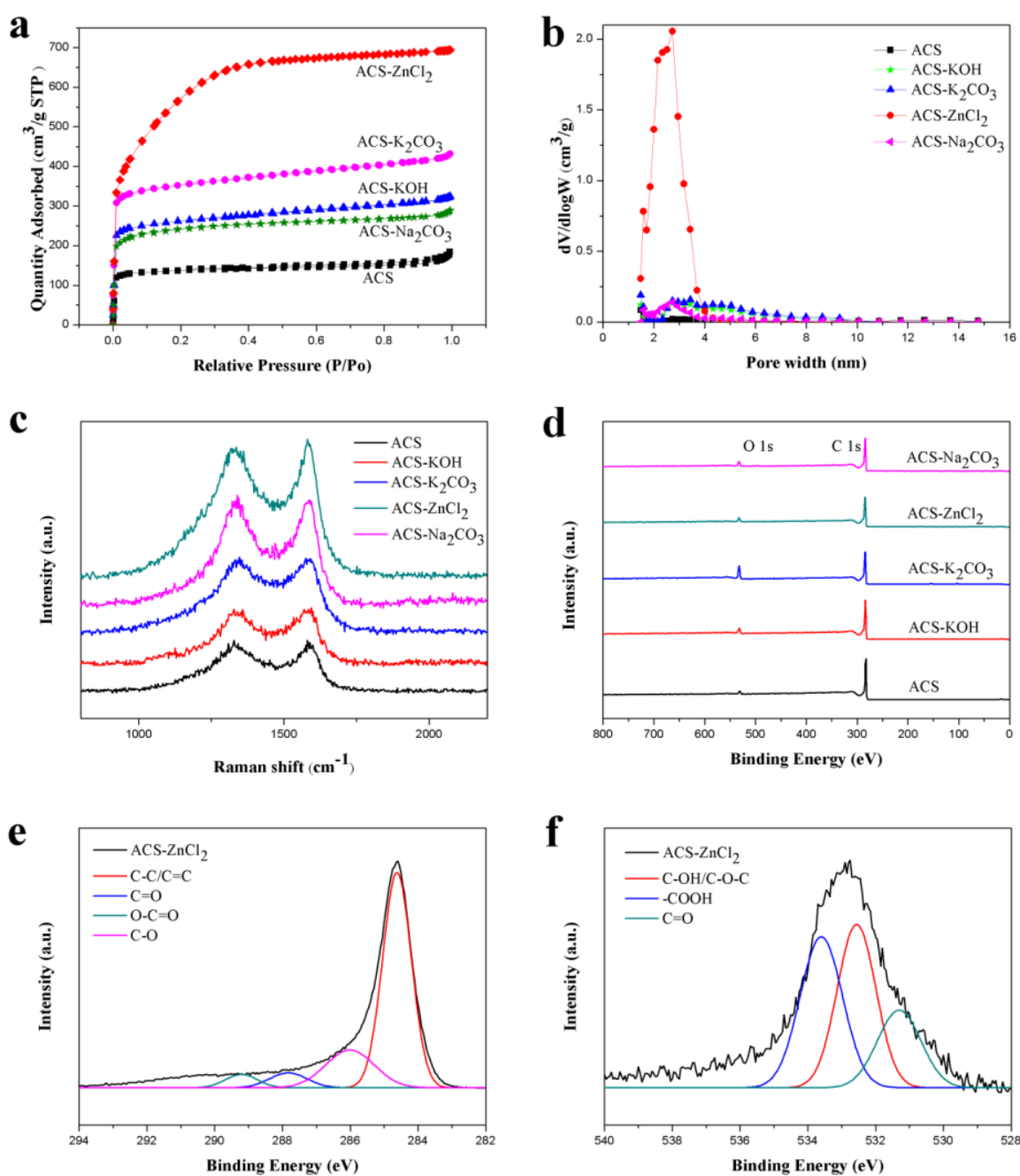


**Figure 3.** (a) N<sub>2</sub> adsorption–desorption isotherms, (b) pore size distributions, (c) Raman spectra, (d) XPS spectra of activated carbon spheres, and XPS spectra of (e) C 1s and (f) O 1s of ACS-ZnCl<sub>2</sub>.

The graphitization degrees of these activated carbon spheres were characterized with Raman spectra (Figure 3c). Two main peaks located at 1330 (D band) and 1590  $\text{cm}^{-1}$  (G band) are related to the disordered carbon and the  $\text{sp}^2$ -hybridized carbon atoms in the graphitic layers, respectively, and the ratio of D and G band intensities ( $I_D/I_G$ ) is usually used to evaluate the degree of graphitization [41–43]. As compared with the  $I_D/I_G$  value of ACS (0.96), the  $I_D/I_G$  values of ACS- $\text{Na}_2\text{CO}_3$ , ACS-KOH, ACS- $\text{K}_2\text{CO}_3$ , and ACS- $\text{ZnCl}_2$  changed slightly, which were 1.03, 0.97, 0.99, and 0.95, respectively. It suggested that the addition of activating reagents did not change the graphitization degrees of these carbon materials significantly under the given conditions.

The surface element compositions of these carbon spheres were further studied with XPS (Figure 3d–f). As shown in Figure 3d, only two peaks at 284.6 eV and 532.8 eV are observed in all samples, which are attributed to the C 1s and O 1s, respectively. The C and O contents of these carbon spheres obtained from the XPS are listed in Table 1. It was found that all these activated carbon spheres contained a large number of C atoms and a small amount of O atoms. As compared with the ACS, the C content of the carbon spheres decreased after activation, while the O content increased to some degree. The reason may be that the activators make more C atoms in the bulk to the surface of carbon materials, which tend to capture more O atoms to form functionalities [15]. The presence of oxygen-containing functional groups can improve the wetting ability of the carbon materials in the electrolytes. Meanwhile, some oxygen-containing functional groups, such as quinone or pyrone groups, may give rise to pseudocapacitance in the supercapacitor, which is beneficial for improving the electrochemical performance of carbon materials [12,44]. Figure 3e and f illustrate the C 1s and O 1s spectra of the ACS- $\text{ZnCl}_2$ , respectively. Four carbon bonds in C 1s spectrum: C–C/C=C (284.6 eV), C–O (286.0 eV), C=O (287.9 eV), and O–C=O (289.2 eV), and three different oxygen bonds in O 1s spectrum: C=O (531.3 eV), C–OH/C–O–C (532.6 eV), and –COOH (533.7 eV) were also observed [11,45].

### 2.3. Electrochemical Properties

The performance of ACS and these activated carbon spheres as electrode materials in a three-electrode system with 6 M KOH aqueous electrolyte was tested to estimate their potential as electrode materials. The electrochemical performances of ACS and these activated carbon spheres were investigated using cyclic voltammetry (CV) and GCD tests, and the corresponding results were presented in Figure 4. As can be seen from Figure 4a, the CV curves of ACS-KOH, ACS- $\text{K}_2\text{CO}_3$ , ACS- $\text{ZnCl}_2$ , and ACS- $\text{Na}_2\text{CO}_3$  were quasi-rectangular at a scan rate of 50 mV/s between –1 and 0 V, implying the good capacitance behavior of these electrode materials. However, a triangle-like CV curve was observed for the ACS. The area under the CV curves decreased in the order of ACS- $\text{ZnCl}_2 \approx$  ACS- $\text{K}_2\text{CO}_3 >$  ACS-KOH  $>$  ACS- $\text{Na}_2\text{CO}_3 >$  ACS. The specific capacitance of ACS- $\text{ZnCl}_2$ , ACS- $\text{K}_2\text{CO}_3$ , ACS-KOH, ACS- $\text{Na}_2\text{CO}_3$ , and ACS electrode from CV curves was 138, 137, 121, 95, and 71 F/g, respectively, suggesting that the ACS- $\text{ZnCl}_2$  and ACS- $\text{K}_2\text{CO}_3$  electrodes possessed relatively high specific capacitance among all the activated carbon sphere electrodes. The GCD curves of these activated carbon spheres are shown in Figure 4b. As illustrated, a distorted triangle-like GCD curve with a huge IR drop was observed from the ACS sample, indicating the big resistance of the ACS sample. However, the GCD curves of the other activated carbon spheres were symmetrical and linearly triangular, and no obvious IR drop was found at the beginning of the discharge process, suggesting the favorable double-layer capacitance behavior and small resistance of these activated carbon spheres. The specific capacitances of these activated carbon spheres in a three-electrode system were calculated from the GCD curves using Equation (1) and shown in Table 1. The specific capacitance of ACS- $\text{ZnCl}_2$  and ACS- $\text{K}_2\text{CO}_3$  electrode was 183 F/g and 172 F/g, respectively, at a current density of 1 A/g, which is much higher than that of the other samples. The orders of the specific capacitance values of these samples were in accordance with their specific surface areas. Additionally, it was found that although the specific surface area of ACS- $\text{ZnCl}_2$  (2025  $\text{m}^2/\text{g}$ ) was much higher than that of ACS- $\text{K}_2\text{CO}_3$  (1141  $\text{m}^2/\text{g}$ ), the specific

capacitances of them were very close. However, a much higher O content can be observed from the ACS-K<sub>2</sub>CO<sub>3</sub> sample (13.45 at.%). Therefore, the specific capacitance of the carbon materials is not only related to the surface areas and porosity but also to their surface functionalities [46].

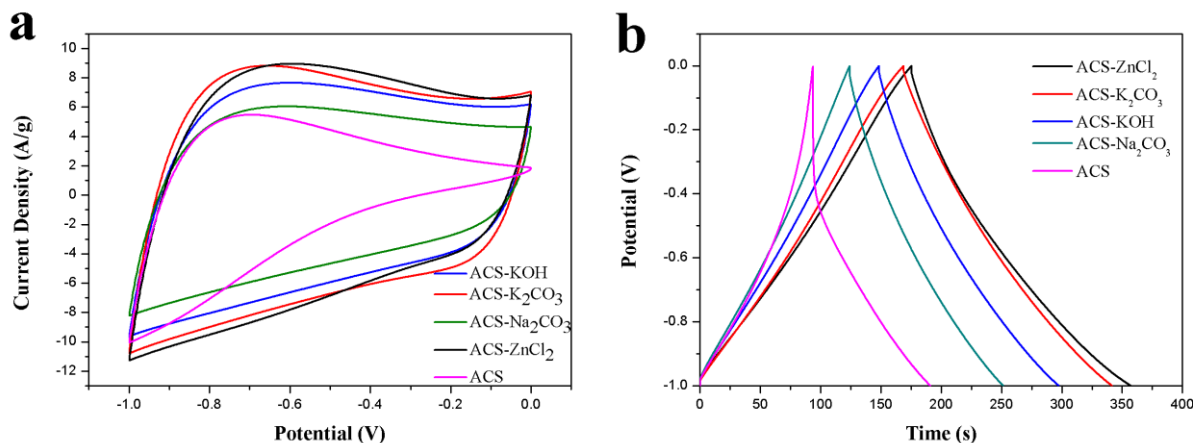


**Figure 4.** (a) CV curves (50 mV/s) and (b) GCD curves (1 A/g) of ACS, ACS-Na<sub>2</sub>CO<sub>3</sub>, ACS-KOH, ACS-K<sub>2</sub>CO<sub>3</sub>, and ACS-ZnCl<sub>2</sub> in 6 M KOH in three-electrode system.

EIS tests were also carried out in the  $10^{-2}$ – $10^5$  Hz frequency range to evaluate the electrochemical impedance of these activated carbon spheres. As shown in Figure S1 of the Supplementary Materials, the near-vertical lines at low frequency represent the dominance of the EDLC, suggesting the good capacitive behavior of these activated carbon spheres. The intercept of the plot with real axis at high frequency is related to the equivalent series resistance (ESR), which includes the ionic resistance of electrolyte, the intrinsic resistance of active materials, and the contact resistance at the interface of active materials and the current collector [29]. A relatively small ESR can be observed for all the activated carbon spheres. The semicircle at the high frequency range is assigned to the charge-transfer resistance ( $R_{ct}$ ) from the interface of active materials and the electrolyte. Results showed that the  $R_{ct}$  of ACS-ZnCl<sub>2</sub> is much higher than other activated carbon spheres. The high  $R_{ct}$  of ACS-ZnCl<sub>2</sub> may be attributed to the poor wettability of the sample with lower O content. Previous works stated that the reasonable specific surface area, balanced pore distribution, appropriate functional groups, and the type of electrolyte could affect the conductivity and ion diffusion rate of the carbon electrode in the electrolyte and cause differences in electrochemical performance between different carbon materials [10]. Combining the results of specific surface area and pore volume of these carbon spheres, it is further confirmed that the existence of large specific surface area and pore volume is conducive to improving the electrochemical properties of carbon materials as electrode materials. The excellent performance of ACS-ZnCl<sub>2</sub> can also be attributed to its developed micro/mesopores structure, since pore structure can facilitate the contact between the electrolyte and the carbon material. Based on the above results, ACS-ZnCl<sub>2</sub> was further explored as an electrode material for the supercapacitor application.

To further optimize the electrochemical performance of ACS-ZnCl<sub>2</sub>, ZnCl<sub>2</sub>-activated carbon spheres were prepared under different ZnCl<sub>2</sub>/hydrothermal carbon spheres weight ratio (1, 2, 3, and 4). The CV and GCD results of these ACS-ZnCl<sub>2</sub> in a three-electrode system were presented in Figure 5a,b, respectively. The results suggested that the specific capacitance of the ACS-ZnCl<sub>2</sub> electrode increases with the dosage of ZnCl<sub>2</sub>. When the mass ratio of ZnCl<sub>2</sub> to hydrothermal carbon spheres is 3:1, the specific capacitance is 183 F/g at 1A/g. However, the specific capacitance (188 F/g) is almost unchanged when the mass ratio of ZnCl<sub>2</sub> to hydrothermal carbon spheres further increases to 4:1. Therefore, the performance of the ACS-ZnCl<sub>2</sub> material obtained at a ZnCl<sub>2</sub>/hydrothermal carbon spheres weight ratio of 3:1 was tested to evaluate the potential of ACS-ZnCl<sub>2</sub> as electrode materials in a three-electrode system with 6 M KOH as the electrolyte, and the results were



shown in Figure 5c–e. The rate performance of ACS-ZnCl<sub>2</sub> electrode was investigated using CV tests at different scan rates. Figure 5c shows that the CV curves exhibit a rectangular-like shape at all scan rates, and the area under the CV curves increases with the scan rates, increasing from 5 to 100 mV/s, suggesting the highly capacitive behavior of the prepared carbon materials with good ion response [47]. GCD curves of the ACS-ZnCl<sub>2</sub> electrode at current densities from 0.2 to 10 A/g (Figure 5d) exhibited a slightly twisted isosceles triangle, and no obvious IR drop was observed at the beginning of the discharge process, indicating the good reversibility of the ACS-ZnCl<sub>2</sub> electrode. The corresponding specific capacitance of the ACS-ZnCl<sub>2</sub> electrode at different current densities is shown in Figure 5e. From the GCD curves, the specific capacitance of the ACS-ZnCl<sub>2</sub> materials obtained at a ZnCl<sub>2</sub>/hydrothermal carbon spheres weight ratio of 3:1 was 218 F/g at a current density of 0.2 A/g. When the current density further increased to 10 A/g, a specific capacitance of 138 F/g was observed. The capacitive performance suggested a good rate capacitive behavior of the ACS-ZnCl<sub>2</sub> materials [23].

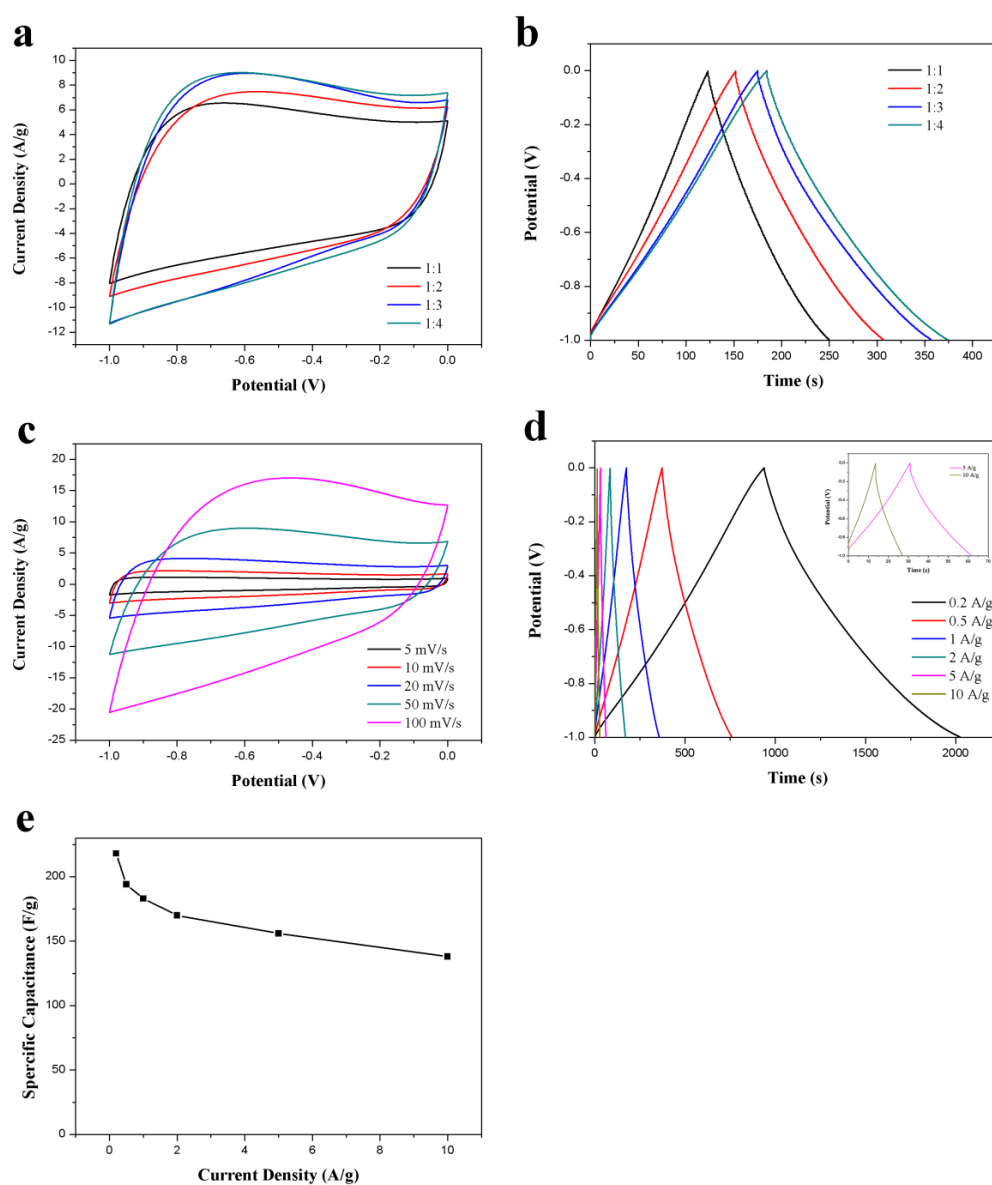


**Figure 5.** (a) CV curves (50 mV/s) and (b) GCD curves (1 A/g) of the activated samples obtained at different mass ratios of carbon spheres to ZnCl<sub>2</sub>; (c) CV curves of the ACS-ZnCl<sub>2</sub> at different scan rates, (d) GCD curves and (e) specific capacitances of the ACS-ZnCl<sub>2</sub> at different current densities. All measurements were performed in 6 M KOH in three-electrode system.



The capacitive performance of the as-prepared ACS-ZnCl<sub>2</sub>-based symmetric supercapacitor was tested for practical application. The supercapacitor was assembled by employing two identical ACS-ZnCl<sub>2</sub> electrodes in 2 M Li<sub>2</sub>SO<sub>4</sub> electrolyte because of the high work potential of the neutral Li<sub>2</sub>SO<sub>4</sub> electrolyte [16]. The CV curves of the ACS-ZnCl<sub>2</sub>-based supercapacitor in the voltage window of 0–1.8 V are shown in Figure 6a. The curve shape was almost unchanged with the increase in the scan rate from 10 to 300 mV/s, revealing a good rate performance of the ACS-ZnCl<sub>2</sub>-based supercapacitor. The GCD curves of the supercapacitor at current densities from 0.5 to 10 A/g are shown in Figure 6b. The IR drop is relatively low, suggesting that the supercapacitor has low internal resistance because of fast ion diffusion and charge transfer. The specific capacitances calculated from the GCD curves are summarized in Figure 6c. It can be seen that the specific capacity decreased with the increase in the current density. The specific capacitance is 137 F/g at 0.5 A/g and decreases to 100 F/g at 10 A/g, indicating a good rate capability of 73% capacitance retention with the growth of current densities from 0.5 to 10 A/g. Based on its high specific capacitance, a high energy density of 15.4 Wh/kg at 0.5A/g was obtained at a power density of 224 W/kg. The energy density of the ACS-ZnCl<sub>2</sub>-based symmetric supercapacitor is higher than that of conventional supercapacitors using activated carbon as the electrode material [5,47]. Moreover, the capacitance retention tests performed at 10 A/g for 2000 cycles are shown in Figure 6d. This suggested that more than 95% capacitance retention was observed after 2000 cycles.

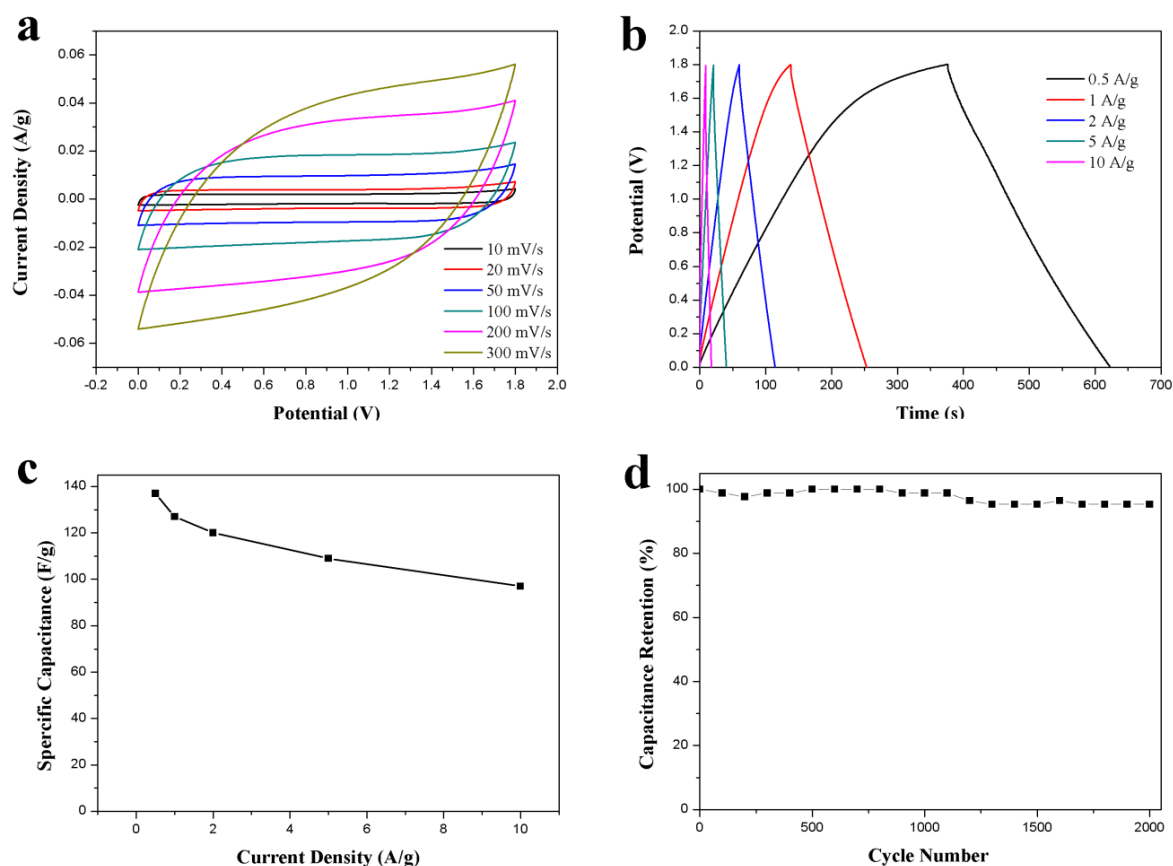


**Figure 6.** Electrochemical performance of the ACS-ZnCl<sub>2</sub> in symmetric supercapacitor in 2 M Li<sub>2</sub>SO<sub>4</sub> electrolyte. (a) CV curves tested at different scan rates, (b) GCD curves and (c) specific capacitances at different current densities, and (d) cycle stability for 2000 cycles at a current density of 10 A/g.

### 3. Materials and Methods

#### 3.1. Materials

The hemicelluloses extracted from the dissolving pulp were supplied by a viscose fiber mill in Xinjiang, China. The preparation of the hemicelluloses can be found in our

previous literature [30]. Potassium carbonate ( $K_2CO_3$ , 99%), potassium hydroxide (KOH, 95%), sodium carbonate ( $Na_2CO_3$ , 99.5%), Zinc chloride ( $ZnCl_2$ , 98%), Lithium sulfate ( $Li_2SO_4$ , 99%), polyvinylidene fluoride (PVDF), N-methyl pyrrolidone (NMP, 99%) were purchased from Shanghai Macklin Biochemical Co., Ltd., Shanghai, China. Acetylene black was obtained from Tianjin Ebory Chemical Co., Ltd., Tianjin, China. Hydrochloric acid (HCl, 37 wt%) and sulfuric acid ( $H_2SO_4$ , 95 wt%) were purchased from Shanghai Chemical Reagent Co., Ltd., Shanghai, China. HCl,  $H_2SO_4$ , KOH,  $K_2CO_3$ ,  $Na_2CO_3$ ,  $ZnCl_2$ ,  $Li_2SO_4$ , PVDF, NMP, and acetylene black were all of analytical grade and used as received.

### 3.2. Preparation of Carbon Spheres from the Hydrothermal Carbonization of Hemicelluloses

Hydrothermal carbonization was used to prepare the carbon spheres from the hemicelluloses. Typically, 3 g of hemicelluloses was placed into a Teflon-lined stainless-steel autoclave with 30 mL 2%  $H_2SO_4$ , and the autoclave was treated at 180 °C for 12 h. After hydrothermal treatment, the autoclave was cooled to room temperature. The mixture was filtered, and the cake was washed with ethanol and water until the filtrate was neutral, then dried at 80 °C for 12 h to obtain the hydrothermal carbon spheres.

### 3.3. Activation of the Hydrothermal Carbon Spheres with Different Activators

A certain amount of hydrothermal carbon spheres was treated with concentrated solutions of different activating reagents (KOH,  $K_2CO_3$ ,  $Na_2CO_3$ , and  $ZnCl_2$ ) for 8 h at the desired mass ratio and then dried in an oven before calcination. A mass ratio of activator to carbon spheres of 3:1 was used, unless specified. The resulting mixture was calcined in a tube furnace at 800 °C for 2 h under the  $N_2$  flow. Finally, the char was thoroughly washed with 1 mol/L HCl solution and deionized water, and dried at 105 °C to obtain the activated carbon spheres.

### 3.4. Characterization of the Prepared Carbon Spheres

The morphology of the carbon spheres was observed using scanning electron microscopy (SEM, JSM-6700F, JEOL Ltd., Tokyo, Japan). The specific surface areas and pore size distribution of carbon spheres were examined using the Micromeritics ASAP 2020 automatic analyzer by  $N_2$  adsorption and desorption of the isotherm at 77 K according to the Brunauer–Emmett–Teller (BET) method and the density functional theory (DFT) model, respectively, and the total pore volume was determined from the adsorption amount of  $N_2$  at a relative pressure of 0.99. Raman spectra of carbon spheres were collected using a LabRam Xplora confocal Raman microscope (Horiba Jobin Yvon, Longjumeau, France) according to a previous paper [48]. The surface chemical species of the carbon spheres were determined by X-ray photoelectron spectroscopy (XPS, ESCALAB 250Xi, Thermo Scientific, Waltham, MA, USA).

### 3.5. Electrochemical Measurements

To measure the electrochemical performance of the obtained carbon spheres, the working electrode of carbon spheres was prepared as follows. The carbon spheres were mixed with acetylene black and PVDF in a weight ratio of 8:1:1 in NMP to form slurries. The slurries were uniformly painted on a 1 cm<sup>2</sup> area of nickel foam, pressed, and dried to obtain the electrode. The electrochemical tests of the electrode were carried out in a three-electrode system using a CHI760e electrochemical workstation (Shanghai Chen Hua Instruments Co., Shanghai, China) in 6 mol/L KOH aqueous solution. Hg/HgO electrode and Pt sheet were used as reference electrode and counter electrode, respectively. CV and GCD were investigated between −1 and 0 V, and the electrochemical impedance spectroscopy (EIS) was collected in a frequency range from 0.01 kHz to 100 kHz with 10 mV amplitude. Specific capacitance ( $C_1$ , F/g) for the single electrode in a three-electrode system was calculated from the discharge curve using Equation (1).

The symmetric supercapacitor was fabricated using two pieces of working electrodes in a 2032-type coin cell with cellulose film as separator and 2 mol/L  $Li_2SO_4$  solution as

electrolyte. The preparation method of the electrode was described as above, and the mass of the carbon spheres loaded on each electrode was about 3 mg. The GCD tests were performed between 0 and 1.8 V at the current densities ranging from 0.5 to 10 A/g. Specific capacitance for the single electrode in the symmetric supercapacitor was calculated from the discharge curve using Equation (2), and the specific energy density ( $E$ , Wh/kg) and specific power density ( $P$ , W/kg) of the symmetric supercapacitor were calculated according to Equations (3) and (4), respectively.

$$C_1 = I \times \Delta t / (m \times \Delta V) \quad (1)$$

$$C = 2I \times \Delta t / (m \times \Delta V) \quad (2)$$

$$E = C \times (\Delta V)^2 / (8 \times 3.6) \quad (3)$$

$$P = 3600 \times E / \Delta t \quad (4)$$

where  $I$  (A) is the discharge current;  $\Delta t$  (s) is the discharge time;  $m$  (g) is the mass of the carbon spheres loaded on each electrode;  $\Delta V$  (V) represents the change of potential during discharge time  $\Delta t$ .

#### 4. Conclusions

This study demonstrated that carbon spheres with excellent electrochemical performance can be obtained from hemicelluloses by hydrothermal carbonization and chemical activation. Activation of these carbon spheres with KOH,  $K_2CO_3$ ,  $Na_2CO_3$ , and  $ZnCl_2$  can significantly improve their specific surface area and pore volume. Among these activated carbon spheres, ACS- $ZnCl_2$ -based symmetric supercapacitor showed a high specific capacitance of 137 F/g at 0.5 A/g in 2 M  $Li_2SO_4$  electrolyte and a large energy density of 15.4 Wh/kg at a power density of 224 W/kg. Moreover, the specific capacitance of the as-assembled symmetric supercapacitor can be retained at more than 95% of the initial specific capacitance at 10 A/g after 2000 cycles.

**Supplementary Materials:** The following supporting information can be downloaded at: <https://www.mdpi.com/article/10.3390/ijms23137101/s1>.

**Author Contributions:** Y.W.: methodology, investigation, writing—original draft; C.L.: methodology; X.C. and J.C.: data curation, formal analysis, supervision, funding acquisition; Q.W.: investigation, funding acquisition; G.Y.: supervision, funding acquisition. All authors have read and agreed to the published version of the manuscript.

**Funding:** This work was supported by the Foundation (No. KF201811) of State Key Laboratory of Biobased Material and Green Papermaking, Qilu University of Technology, Shandong Academy of Sciences, the National Natural Science Foundation of China (31700518, 31770628), the Outstanding Youth Innovation Team Project of Shandong Provincial University (2019KJC014), and Pilot project for integrating science, education and industry (2020KJC-ZD14).

**Institutional Review Board Statement:** Not applicable.

**Informed Consent Statement:** Not applicable.

**Data Availability Statement:** The data presented in this study are available on request from the corresponding authors.

**Conflicts of Interest:** The authors declare no conflict of interest.

#### References

1. Lin, T.; Chen, I.W.; Liu, F.; Yang, C.; Bi, H.; Xu, F.; Huang, F. Nitrogen-doped mesoporous carbon of extraordinary capacitance for electrochemical energy storage. *Science* **2015**, *350*, 1508–1513. [[CrossRef](#)] [[PubMed](#)]
2. Subramanian, V.; Luo, C.; Stephan, A.M.; Nahm, K.; Thomas, S.; Wei, B. Supercapacitors from activated carbon derived from banana fibers. *J. Phys. Chem. C* **2007**, *111*, 7527–7531. [[CrossRef](#)]
3. Yu, M.; Han, Y.; Li, Y.; Li, J.; Wang, L. Polypyrrole-anchored cattail biomass-derived carbon aerogels for high performance binder-free supercapacitors. *Carbohydr. Polym.* **2018**, *199*, 555–562. [[CrossRef](#)] [[PubMed](#)]

4. Zhang, L.L.; Zhao, X. Carbon-based materials as supercapacitor electrodes. *Chem. Soc. Rev.* **2009**, *38*, 2520–2531. [[CrossRef](#)] [[PubMed](#)]
5. Kim, T.; Jung, G.; Yoo, S.; Suh, K.S.; Ruoff, R.S. Activated graphene-based carbons as supercapacitor electrodes with macro- and mesopores. *ACS Nano* **2013**, *7*, 6899–6905. [[CrossRef](#)] [[PubMed](#)]
6. Cao, Q.; Zhang, Y.; Chen, J.; Zhu, M.; Yang, C.; Guo, H.; Song, Y.; Li, Y.; Zhou, J. Electrospun biomass based carbon nanofibers as high-performance supercapacitors. *Ind. Crops Prod.* **2020**, *148*, 112181. [[CrossRef](#)]
7. Li, X.; Zhang, W.; Wu, M.; Li, S.; Li, X.; Li, Z. Multiple-heteroatom doped porous carbons from self-activation of lignosulfonate with melamine for high performance supercapacitors. *Int. J. Biol. Macromol.* **2021**, *183*, 950–961. [[CrossRef](#)]
8. Xia, J.; Zhang, N.; Chong, S.; Chen, Y.; Sun, C. Three-dimensional porous graphene-like sheets synthesized from biocarbon via low-temperature graphitization for a supercapacitor. *Green Chem.* **2018**, *20*, 694–700. [[CrossRef](#)]
9. Viggì, C.C.; Simonetti, S.; Palma, E.; Pagliaccia, P.; Braguglia, C.; Fazi, S.; Baronti, S.; Navarra, M.A.; Pettiti, I.; Koch, C.; et al. Enhancing methane production from food waste fermentate using biochar: The added value of electrochemical testing in pre-selecting the most effective type of biochar. *Biotechnol. Biofuels* **2017**, *10*, 303. [[CrossRef](#)]
10. Li, Z.; Guo, D.; Liu, Y.; Wang, H.; Wang, L. Recent advances and challenges in biomass-derived porous carbon nanomaterials for supercapacitors. *Chem. Eng. J.* **2020**, *397*, 125418. [[CrossRef](#)]
11. Pang, J.; Zhang, W.; Zhang, J.; Cao, G.; Han, M.; Yang, Y. Facile and sustainable synthesis of sodium lignosulfonate derived hierarchical porous carbons for supercapacitors with high volumetric energy densities. *Green Chem.* **2017**, *19*, 3916–3926. [[CrossRef](#)]
12. Yang, J.; Wang, Y.; Luo, J.; Chen, L. Highly nitrogen-doped graphitic carbon fibers from sustainable plant protein for supercapacitor. *Ind. Crops Prod.* **2018**, *121*, 226–235. [[CrossRef](#)]
13. Wang, S.; Dong, L.; Li, Z.; Lin, N.; Xu, H.; Gao, S. Sustainable supercapacitors of nitrogen-doping porous carbon based on cellulose nanocrystals and urea. *Int. J. Biol. Macromol.* **2020**, *164*, 4095–4103. [[CrossRef](#)]
14. Min, J.; Xu, X.; Li, J.; Ma, C.; Gong, J.; Wen, X.; Chen, X.; Azadmanjiri, J.; Tang, T. Sustainable polylysine conversion to nitrogen-containing porous carbon flakes: Potential application in supercapacitors. *J. Appl. Polym. Sci.* **2019**, *136*, 48214. [[CrossRef](#)]
15. Wang, Y.; Yang, R.; Li, M.; Zhao, Z. Hydrothermal preparation of highly porous carbon spheres from hemp (*Cannabis sativa* L.) stem hemicellulose for use in energy-related applications. *Ind. Crops Prod.* **2015**, *65*, 216–226. [[CrossRef](#)]
16. Zou, K.; Deng, Y.; Chen, J.; Qian, Y.; Yang, Y.; Li, Y.; Chen, G. Hierarchically porous nitrogen-doped carbon derived from the activation of agriculture waste by potassium hydroxide and urea for high-performance supercapacitors. *J. Power Sources* **2018**, *378*, 579–588. [[CrossRef](#)]
17. Liu, S.; Zhao, Y.; Zhang, B.; Xia, H.; Zhou, J.; Xie, W.; Li, H. Nano-micro carbon spheres anchored on porous carbon derived from dual-biomass as high rate performance supercapacitor electrodes. *J. Power Sources* **2018**, *381*, 116–126. [[CrossRef](#)]
18. Zhao, X.; Chen, H.; Kong, F.; Zhang, Y.; Wang, S.; Liu, S.; Lucia, L.A.; Fatehi, P.; Pang, H. Fabrication, characteristics and applications of carbon materials with different morphologies and porous structures produced from wood liquefaction: A review. *Chem. Eng. J.* **2019**, *364*, 226–243. [[CrossRef](#)]
19. Yi, Z.J.; Chao, G.; Wen, K.H.; Zhu, Y.; Huczko, A.; Bystrzejewski, M.; Roe, M.; Chi, Y.L.; Acquah, S.; Kroto, H. Large-scale synthesis and characterization of carbon spheres prepared by direct pyrolysis of hydrocarbons. *Carbon* **2005**, *43*, 1944–1953.
20. Saengsrirachan, A.; Saikate, C.; Silasana, P.; Khemthong, P.; Wanmolee, W.; Phanthasri, J.; Youngjan, S.; Posoknistakul, P.; Ratchahat, S.; Laosiripojana, N.; et al. The Role of N and S Doping on Photoluminescent Characteristics of Carbon Dots from Palm Bunches for Fluorimetric Sensing of Fe<sup>3+</sup> Ion. *Int. J. Mol. Sci.* **2022**, *23*, 5001. [[CrossRef](#)]
21. Falco, C.; Sieben, J.M.; Brun, N.; Sevilla, M.; van der Maelen, T.; Morallón, E.; Cazorla-Amorós, D.; Titirici, M.M. Hydrothermal carbons from hemicellulose-derived aqueous hydrolysis products as electrode materials for supercapacitors. *ChemSusChem* **2013**, *6*, 374–382. [[CrossRef](#)] [[PubMed](#)]
22. Inada, M.; Enomoto, N.; Hojo, J.; Hayashi, K. Structural analysis and capacitive properties of carbon spheres prepared by hydrothermal carbonization. *Adv. Powder Technol.* **2017**, *28*, 884–889. [[CrossRef](#)]
23. Tang, D.; Luo, Y.; Lei, W.; Xiang, Q.; Ren, W.; Song, W.; Chen, K.; Sun, J. Hierarchical porous carbon materials derived from waste lentinus edodes by a hybrid hydrothermal and molten salt process for supercapacitor applications. *Appl. Surf. Sci.* **2018**, *462*, 862–871. [[CrossRef](#)]
24. Tong, X.; Chen, Z.; Zhuo, H.; Hu, Y.; Jing, S.; Liu, J.; Zhong, L. Tailoring the physicochemical properties of chitosan-derived N-doped carbon by controlling hydrothermal carbonization time for high-performance supercapacitor application. *Carbohydr. Polym.* **2019**, *207*, 764–774. [[CrossRef](#)] [[PubMed](#)]
25. Sevilla, M.; Mokaya, R. Energy storage applications of activated carbons: Supercapacitors and hydrogen storage. *Energy Environ. Sci.* **2014**, *7*, 125–128. [[CrossRef](#)]
26. Romero-Anaya, A.J.; Ouzzine, M.; Lillo-Ródenas, M.A.; Linares-Solano, A. Spherical carbons: Synthesis, characterization and activation processes. *Carbon* **2014**, *68*, 296–307. [[CrossRef](#)]
27. Shu, Y.; Bai, Q.; Fu, G.; Xiong, Q.; Li, C.; Ding, H.; Shen, Y.; Uyama, H. Hierarchical porous carbons from polysaccharides carboxymethyl cellulose, bacterial cellulose, and citric acid for supercapacitor. *Carbohydr. Polym.* **2020**, *227*, 115346. [[CrossRef](#)]
28. Rey-Raap, N.; Enterría, M.; Martins, J.I.; Pereira, M.F.R.; Figueiredo, J.L. Influence of multiwalled carbon nanotubes as additives in biomass-derived carbons for supercapacitor applications. *ACS Appl. Mater. Interfaces* **2019**, *11*, 6066–6077. [[CrossRef](#)]



29. Fan, Y.; Yang, X.; Zhu, B.; Liu, P.; Lu, H. Micro-mesoporous carbon spheres derived from carrageenan as electrode material for supercapacitors. *J. Power Sources* **2014**, *268*, 584–590. [[CrossRef](#)]
30. Wang, Y.; Cao, X.; Zhang, R.; Xiao, L.; Yuan, T.; Shi, Q.; Sun, R. Evaluation of xylooligosaccharide production from residual hemicelluloses of dissolving pulp by acid and enzymatic hydrolysis. *RSC Adv.* **2018**, *8*, 35211–35217. [[CrossRef](#)]
31. Reiche, S.; Kowalew, N.; Schlögl, R. Influence of synthesis pH and oxidative strength of the catalyzing acid on the morphology and chemical structure of hydrothermal carbon. *ChemPhysChem* **2015**, *16*, 579–587. [[CrossRef](#)] [[PubMed](#)]
32. Martín-Jimeno, F.J.; Suárez-García, F.; Paredes, J.I.; Martínez-Alonso, A.; Tascón, J.M.D. Activated carbon xerogels with a cellular morphology derived from hydrothermally carbonized glucose-graphene oxide hybrids and their performance towards CO<sub>2</sub> and dye adsorption. *Carbon* **2015**, *81*, 137–147. [[CrossRef](#)]
33. Thommes, M.; Kaneko, K.; Neimark, A.V.; Olivier, J.P.; Rodriguez-Reinoso, F.; Rouquerol, J.; Sing, K.S.W. Physisorption of gases, with special reference to the evaluation of surface area and pore size distribution (IUPAC Technical Report). *Pure Appl. Chem.* **2015**, *87*, 1051–1069. [[CrossRef](#)]
34. Xu, B.; Hou, S.; Cao, G.; Wu, F.; Yang, Y. Sustainable nitrogen-doped porous carbon with high surface areas prepared from gelatin for supercapacitors. *J. Mater. Chem.* **2012**, *22*, 19088. [[CrossRef](#)]
35. Heidarinejad, Z.; Dehghani, M.H.; Heidari, M.; Javedan, G.; Ali, I.; Sillanpää, M. Methods for preparation and activation of activated carbon: A review. *Environ. Chem. Lett.* **2020**, *18*, 393–415. [[CrossRef](#)]
36. Rupar, J.; Bajuk-Bogdanović, D.; Milojević-Rakić, M.; Krstić, J.; Upadhyay, K.; Gavrilov, N.; Ležaić, A.J. Tailored porosity development in carbons via Zn<sup>2+</sup> monodispersion: Fitting supercapacitors. *Micropor. Mesopor. Mat.* **2022**, *335*, 111790. [[CrossRef](#)]
37. Ahmadpour, A.; Do, D.D. The preparation of activated carbon from macadamia nutshell by chemical activation. *Carbon* **1997**, *35*, 1723–1732. [[CrossRef](#)]
38. Molina-Sabio, M.; Rodriguez-Reinoso, F. Role of chemical activation in the development of carbon porosity. *Colloid. Surf. A* **2004**, *241*, 15–25. [[CrossRef](#)]
39. Dutta, S.; Bhaumik, A.; Wu, K.C.W. Hierarchically porous carbon derived from polymers and biomass: Effect of interconnected pores on energy applications. *Energy Environ. Sci.* **2014**, *7*, 3574–3592. [[CrossRef](#)]
40. Hou, J.; Cao, C.; Idrees, F.; Ma, X. Hierarchical porous nitrogen-doped carbon nanosheets derived from silk for ultrahigh-capacity battery anodes and supercapacitors. *ACS Nano* **2015**, *9*, 2556–2564. [[CrossRef](#)]
41. Ferrari, A.C.; Robertson, J. Interpretation of Raman spectra of disordered and amorphous carbon. *Phys. Rev. B* **2000**, *61*, 14095. [[CrossRef](#)]
42. Ferrari, A.C.; Robertson, J. Resonant Raman spectroscopy of disordered, amorphous, and diamondlike carbon. *Phys. Rev. B* **2001**, *64*, 075414. [[CrossRef](#)]
43. Xie, Q.; Bao, R.; Zheng, A.; Zhang, Y.; Wu, S.; Xie, C.; Zhao, P. Sustainable low-cost green electrodes with high volumetric capacitance for aqueous symmetric supercapacitors with high energy density. *ACS Sustain. Chem. Eng.* **2016**, *4*, 1422–1430. [[CrossRef](#)]
44. Hao, L.; Li, X.; Zhi, L. Carbonaceous electrode materials for supercapacitors. *Adv. Mater.* **2013**, *25*, 3899–3904. [[CrossRef](#)]
45. Desimoni, E.; Casella, G.; Salvi, A. XPS/XAES study of carbon fibres during thermal annealing under UHV conditions. *Carbon* **1992**, *30*, 521–526. [[CrossRef](#)]
46. Pandolfo, A.G.; Hollenkamp, A.F. Carbon properties and their role in supercapacitors. *J. Power Sources* **2006**, *157*, 11–27. [[CrossRef](#)]
47. Zhu, Y.; Chen, M.; Zhang, Y.; Zhao, W.; Wang, C. A biomass-derived nitrogen-doped porous carbon for high-energy supercapacitor. *Carbon* **2018**, *140*, 404–412. [[CrossRef](#)]
48. Li, H.Y.; Sun, S.N.; Wang, C.Z.; Sun, R.C. Structural and dynamic changes of lignin in Eucalyptus cell walls during successive alkaline ethanol treatments. *Ind. Crops Prod.* **2015**, *74*, 200–208. [[CrossRef](#)]